Response of the Baiu Rainband to Northwest Pacific SST Anomalies and Its Impact on Atmospheric Circulation

SHINJI MATSUMURA AND TAKESHI HORINOUCHI

Faculty of Environmental Earth Science, Hokkaido University, Sapporo, Japan

SHIORI SUGIMOTO

Japan Agency for Marine-Earth Science and Technology, Yokosuka, Japan

TOMONORI SATO

Faculty of Environmental Earth Science, Hokkaido University, Sapporo, Japan

ABSTRACT

The Pacific–Japan (PJ) teleconnection pattern leads to a meridional precipitation dipole between the subtropics and East Asia in the summer of El Niño decaying years. However, observational analysis and model experiments indicate that increased sea surface temperature (SST) in the Kuroshio–Oyashio Extension (KOE) region, where a strong northward-decreasing SST gradient occurs, induces a northward shift of baiu rainfall with the subtropical jet, forming a tripolar precipitation anomaly pattern over the northwest Pacific. In July, the leading empirical orthogonal function (EOF) mode for precipitation represents the meridional dipole between subtropical and baiu rainfalls, while EOF-2 features the northward-shifted baiu rainband. The PJ atmospheric forcing increases KOE SST, which enhances northward shifts in the subtropical jet and baiu rainband, resulting in oceanic forcing over the KOE. In experiments using a regional climate model the subtropical jet response to KOE SST forcing explains about 20% of the anomalies in the control experiment. The northward-shifted baiu condensational heating also enhances the northward shift of the subtropical jet with a northeastward extension. In August when the baiu rainband disappears, the northward shift of the subtropical jet is enhanced mainly by KOE SST variability. During the summer, as a result of increased KOE SST and the northward-shifted baiu heating, cyclonic anomalies intensify over the Sea of Okhotsk and anticyclonic anomalies intensify over the northwest Pacific, affecting the western Pacific subtropical high. The results suggest that air–sea interaction over the KOE must be considered to better understand the summer northwest Pacific climate.

1. Introduction

The East Asian summer monsoon (EASM) extends from East Asia to the northwest (NW) Pacific. Note that in the NW Pacific, we refer to the EASM as baiu-rainband activity to distinguish between East Asia and the NW Pacific. Summer rainfall variability is of great socioeconomic importance for East Asia. Baiu/EASM rainfall variability is determined mainly by the so-called Pacific–Japan (PJ) meridional teleconnection pattern

(Nitta 1987; Kurihara and Tsuyuki 1987). Over the tropical Indian Ocean following El Niño, increased sea surface temperature (SST) excites a warm Kelvin wave in tropospheric temperature, resulting in NW Pacific climate anomalies (e.g., Xie et al. 2009; Huang et al. 2010; Chowdary et al. 2011). The tropical Indian Ocean SST anomalies act as the anchor of the PJ pattern via the capacitor effect. Since the 1980s, the tropical Indian Ocean SST forcing of the PJ pattern has strengthened, resulting in increased El Niño–Southern Oscillation (ENSO) influence on baiu/EASM rainfall (Xie et al. 2010). Over the NW Pacific, however, baiu-rainband activity has strengthened and shifted northward in the past three decades, leading to weakening of the Okhotsk high and intensification of the western Pacific

Corresponding author address: Shinji Matsumura, Faculty of Environmental Earth Science, Hokkaido University, Kita 10 Nishi 5, Sapporo 060-0810, Japan.
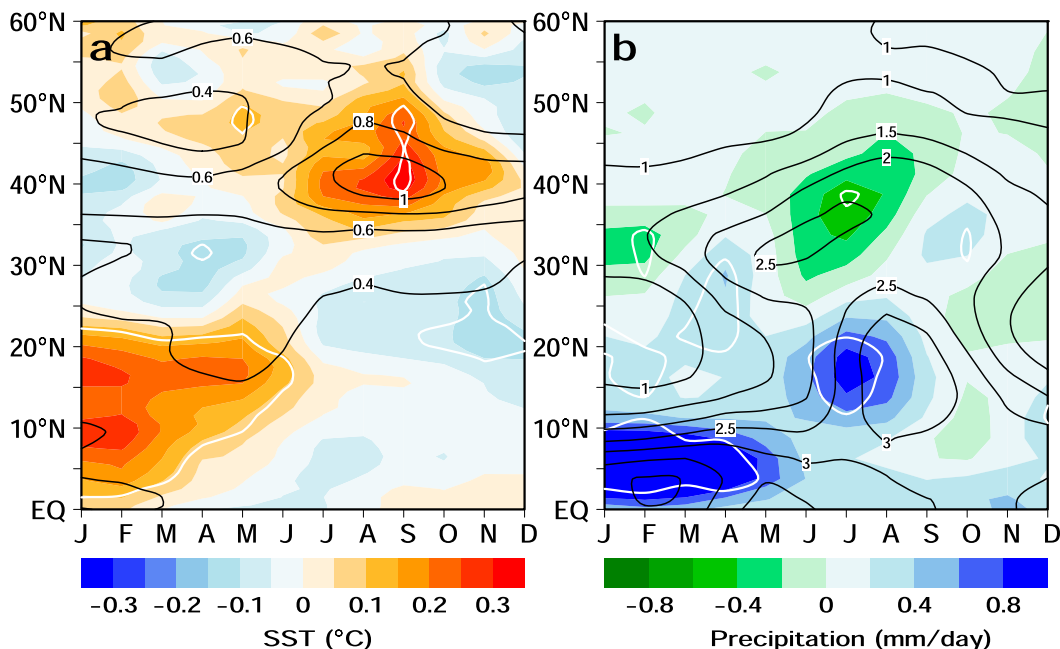E-mail: matsusnj@ees.hokudai.ac.jp

FIG. 1. Time–latitude section of regression on the preceding NDJ (November–January) Niño-3.4 SST index as a function of year and calendar month for the decay year of ENSO: (a) SST over the NW Pacific (145°–165°E) and (b) precipitation over 140°–160°E for the period 1982–2012, based on HadSST and GPCP, respectively. Note that the polarity of ENSO is reversed to emphasize La Niña. White contours indicate statistical significance at the 90% level and thin black contours indicate standard deviation.

subtropical high (WPSH) (Matsumura et al. 2015a). The cause of the northward shift of the baiu rainband remains unclear. We, therefore, focus on the interannual variability of the baiu rainband, as it is easier to investigate than the long-term changes.

Figure 1 shows the regressions of SST and precipitation against ENSO in its decaying phase over the NW Pacific; this extends Fig. 9 in Xie et al. (2009) to higher latitudes and a wider range of longitudes. Note that the polarity of ENSO in our analysis is reversed to emphasize La Niña. Over 0°–10°N, La Niña–induced positive SST and precipitation anomalies decay rapidly in spring. The positive precipitation anomalies jump to 10°–20°N in June, but are not associated with significant SST anomalies, appearing to result instead from thermally indirect forcing. Simultaneously, ENSO-induced negative precipitation anomalies appear over 30°–40°N, indicating that the meridional dipole between subtropical and baiu rainfalls can be explained as a result of the ENSO-induced PJ pattern.

ENSO-induced positive SST anomalies are also seen in the Kuroshio–Oyashio Extension (KOE) region where there is a strong northward-decreasing climatological SST gradient, and summer SST variance is strongest. Although the precipitation dipole is most pronounced in July, the KOE SST anomalies are strongest in late summer, causing a time lag between the PJ pattern and SST anomalies. In the tropics and subtropics, ENSO-induced positive SST anomalies have approximately the same magnitude as the SST variance, while the summer KOE SST anomalies are much weaker than their variance. Thus, atmospheric forcings, such as the PJ pattern and the WPSH, can be responsible for the primary drivers of the KOE SST anomalies, because the thermocline is shallow in summer (e.g., Kwon et al. 2010). In summer in the KOE region, however, the meridional shifts in the KOE SST front lead to a shift in the subtropical jet by modifying the near-surface baroclinic atmosphere and affect the atmospheric circulation (Nakamura and Yamane 2010; Nakamura and Miyama 2014), even if the ENSO signal is removed (Frankignoul and Sennechael 2007; Frankignoul et al. 2011), thereby causing an oceanic forcing in the summer KOE when the thermocline is shallowest. Therefore, the ENSO-induced PJ pattern (Fig. 1) might not satisfactorily capture the midlatitude atmospheric response to oceanic forcing. Indeed, recent tripolar-like precipitation changes (Matsumura et al. 2015a) are not seen in Fig. 1, and the baiu rainfall response to KOE SST forcing remains unclear.

Although the ENSO-induced PJ pattern leads to the meridional dipole between subtropical and baiu rainfall,
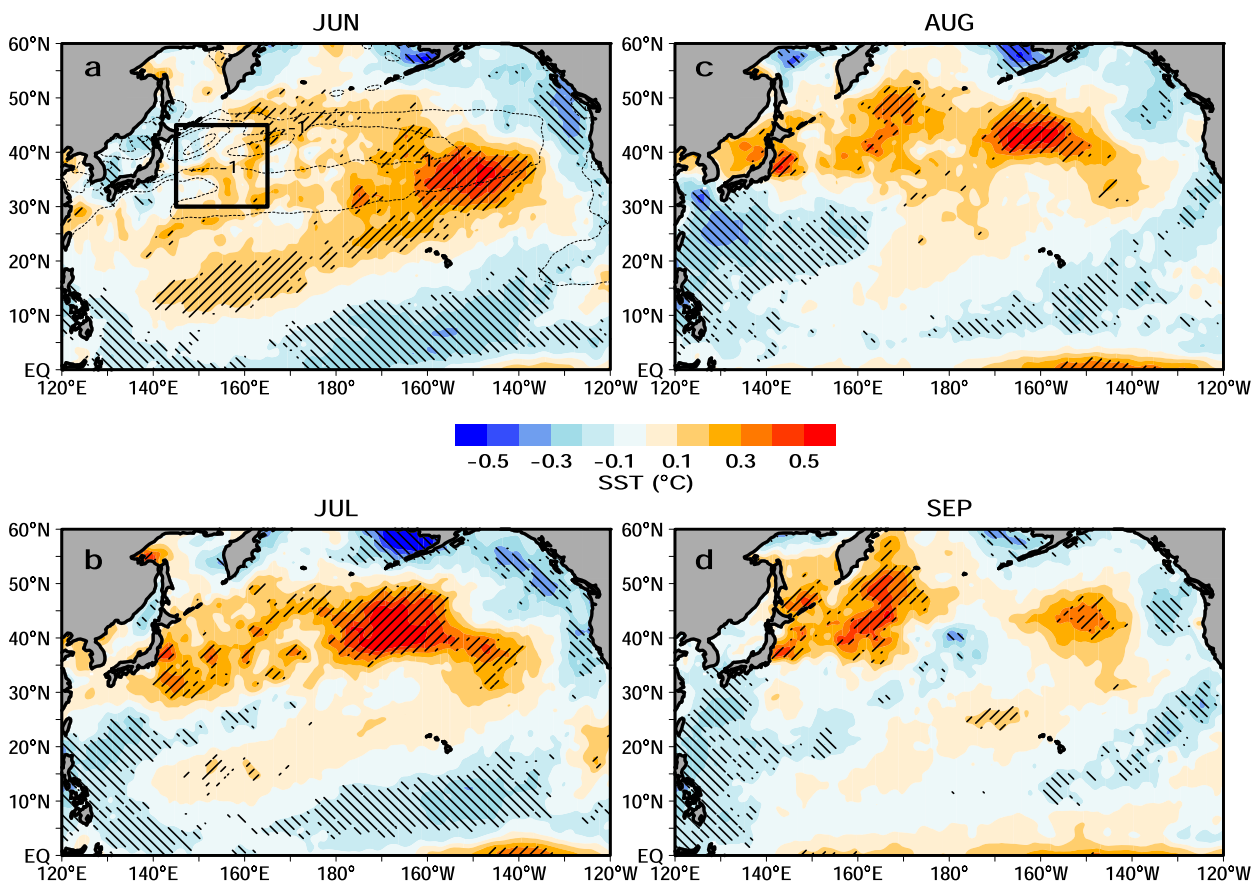
FIG. 2. Regression of summer SST (°C) on the preceding NDJ Niño-3.4 SST index in (a) June, (b) July, (c) August, and (d) September based on OISST. Hatched regions indicate statistical significance at the 90% level. Thick black rectangle shows the region of the KOE SST index (30°–45°N, 145°–165°E) used in this study. Thin dotted contours indicate summer (JJA) mean meridional SST gradient [0.5°C $(25\,km)^{-1}$ contour interval].

the baiu rainband also plays an important role in the connection between the subtropics and midlatitudes by enhancing the PJ pattern (Lu and Lin 2009; Hirota and Takahashi 2012). Thus, in addition to the KOE SST forcing, we also need to consider the role of baiu-rainband activity in the PJ pattern. The present study attempts to elucidate the response of baiu rainfall to KOE SST variability and the roles of baiu rainfall and KOE SST in the summer atmospheric circulation, using observations and model experiments. We focus on the role of the ocean in air–sea interaction, and the role of moist processes in the baiu rainband. Since baiu-rainband activity is interactively linked with the WPSH through the lower-tropospheric southwest-erlies, it is difficult to isolate the impact of baiu forcing, or to simulate baiu-rainband activity in global climate models (Ninomiya et al. 2002; Ninomiya 2009). In previous studies, idealized model experiments were performed to clarify the impacts of baiu (Lu and Lin 2009; Sampe and Xie 2010) and KOE SST (Nakamura

and Miyama 2014) forcings in the summer atmospheric circulation, because of the difficulty in obtaining a ro-bust atmospheric response to those forcings in realistic model experiments, especially in global climate models. Here and in an earlier study (Matsumura et al. 2015a) realistic long-term numerical experiments are per-formed using a regional climate model that can simulate baiu-rainband activity better than global climate models. Our model experiments can also isolate the atmospheric responses to baiu and KOE SST forcings in the realistic interannual variability. The model experiments focus on long-term changes in the earlier study but on interannual variability here.

The remainder of this paper is organized as follows. Section 2 describes the data and model experiments. Section 3 defines the KOE SST index, presents pre-cipitation responses to ENSO and KOE SST, and dis-cusses the atmospheric responses based on observational diagnosis. Section 4 examines atmospheric responses to baiu heating and KOE SST using a regional climate
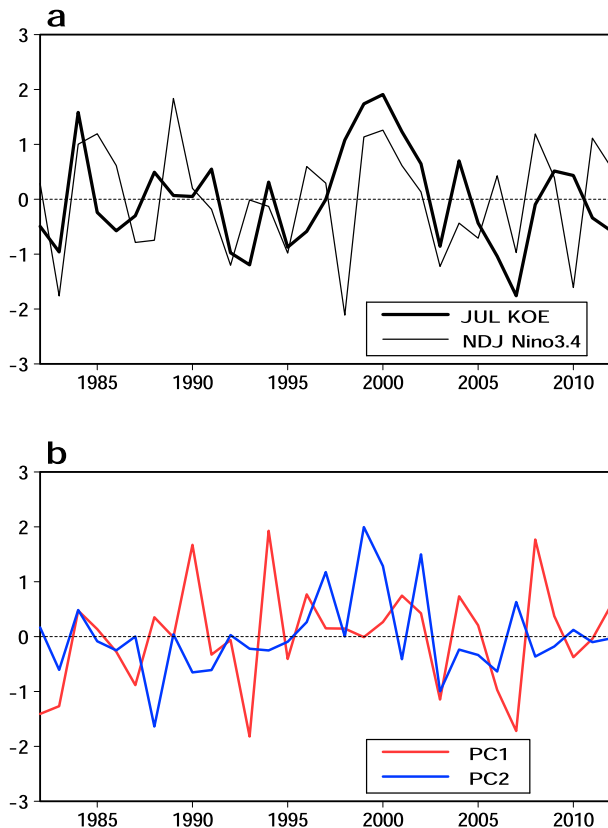
FIG. 3. (a) Normalized time series of July KOE SST index and NDJ Niño-3.4 SST index. (b) PC-1 and PC-2 of precipitation over 20°–60°N, 100°E–180° in July.

model. Finally, a discussion of the results and the main conclusions are given in section 5.

2. Data and model

a. Data

We used the European Centre for Medium-Range Weather Forecasts interim reanalysis (ERA-Interim; Dee et al. 2011), the Global Precipitation Climatology Project (GPCP; Huffman et al. 1997), the Hadley Centre Global Sea Surface Temperature (HadSST; Rayner et al. 2006), and the National Oceanic and Atmospheric Administration optimal interpolation SST (OISST; Reynolds et al. 2007) datasets. Following Xie et al. (2009), we use November–January (NDJ) HadSST averaged over the eastern equatorial Pacific (Niño-3.4: 5°S–5°N, 120°–170°W) to track ENSO, and refer to this as the ENSO index. Note that the polarity of ENSO in our analysis is reversed to emphasize La Niña (see Fig. 3a). Our study covers the past three decades (1982–2012), for which high-resolution OISST is available, and focuses on interannual variability, which is identified using linearly detrended data.

b. Model and experimental design

The model used in this study is the Weather Research and Forecasting (WRF) Model version 3.2.1 with the Advanced Research WRF dynamical core (Skamarock et al. 2008). We used realistic long-term experimental results (CTRL and NOMP runs) from Matsumura et al. (2015a), which were obtained using cumulus parameterization (Grell and Dévényi 2002) and cloud microphysics (Hong et al. 2004) for the cloud scheme. The model domain focuses on the NW Pacific poleward of 30°N with a horizontal resolution of 25 km (170 × 150 grid) and 40 vertical layers. The 6-hourly data of the ERA-Interim reanalysis were used as the atmospheric lateral boundary conditions. The daily mean OISST with a 0.25° grid was used as the ocean surface boundary condition. Model integrations were conducted from 20 May to 31 August for the period 1982–2012 (CTRL run).

To elucidate the atmospheric response to baiu condensational heating, we turned off latent heating from the cloud microphysics scheme within the entire model domain while retaining latent heating from the cumulus parameterization. This sensitivity experiment (hereafter the NOMP run) was conducted under the same model configuration as the CTRL run. The NOMP run removes the effect of latent heating from the cloud microphysics scheme but has little effect on the cumulus precipitation, because our model domain is limited. Thus, compared with the CTRL run, the NOMP run not only suppresses diabatic heating (hereafter baiu heating) associated with the actual distribution of condensation, but also the effect of any dynamical change due to the existence of condensation heating. To remove the effect of the interannual variability of SST forcing, in this study additional experiments with prescribed climatological SST were performed (hereafter the CLIM run) with the same model configuration as the CTRL run.

3. Observational analysis

a. Precipitation responses to ENSO and KOE SST

Figure 2 shows the ENSO decaying phase regressions of summer SST using OISST with 0.25° resolution. Overall, La Niña–induced SST anomalies closely resemble the negative phase of the Pacific decadal oscillation (PDO; Mantua et al. 1997). Although spring is the season when ENSO is in rapid decay, SST anomalies in June remain negative in the tropical eastern Pacific and positive in the subtropical NW Pacific, while in the KOE there is only a small pronounced SST anomaly. In July, positive SST anomalies rapidly weaken in the
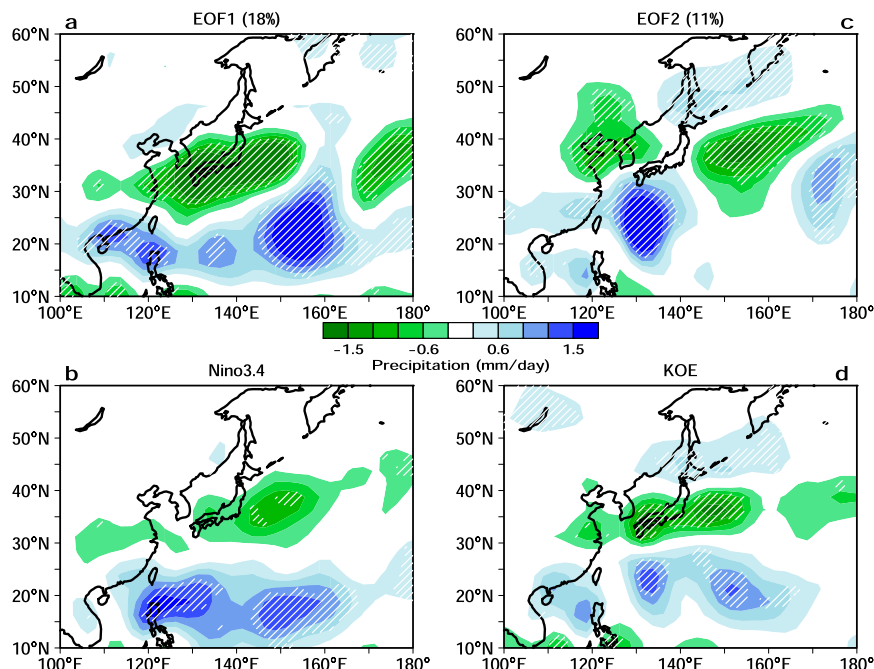
FIG. 4. July precipitation anomalies (mm day^{-1}) regressed on (a) PC-1 and (c) PC-2 of precipitation over 20°–60°N, 100°E–180°, (b) the preceding NDJ Niño-3.4 SST index, and (d) the July KOE SST index. Hatched regions indicate statistical significance at the 95% level.

subtropical NW Pacific, where convection rapidly develops (Ueda et al. 1995), while in the KOE they strengthen north of 30°N. The increased KOE SST anomalies persist north of 35°N in August, reaching a maximum in September. In the tropical and subtropical NW Pacific, negative SST anomalies strengthen, leading to a contrasting response north and south of 30°N in July and 35°N in August and September. The north–south contrasting SST anomalies can be explained as a result of the ENSO-induced PJ pattern (Xie et al. 2009), which leads to an anticyclonic circulation over the KOE including Japan and a cyclonic circulation in the subtropics (e.g., Kosaka et al. 2012). The increased KOE SST anomalies strengthen rapidly in July when baiu-rainband activity over the NW Pacific is most active, although the thermocline in the KOE is shallowest in August and thermocline feedback is strong (e.g., Kwon et al. 2010).

To examine the atmospheric response to KOE SST variability, we define the KOE SST index averaged over 30°–45°N, 145°–165°E (thick black box in Fig. 2a) using OISST, because ENSO-induced positive SST anomalies are strengthened in this region. In the KOE, the atmospheric response derived from SST variability reflects its response to the meridional SST gradient (Nakamura and Miyama 2014). In the

remainder of this paper, we discuss the responses of the baiu rainband and atmospheric circulation to the KOE SST index.

Before examining the impact of the KOE SST index, we first perform an empirical orthogonal function (EOF) analysis of precipitation over 20°–60°N, 100°E–180° in July, when the precipitation dipole is the most significant (Fig. 1b) and the climatological baiu rainband is located along 40°N. Figures 4a and 4c show precipitation anomalies regressed on the first and second principal components (PC) (Fig. 3b), which explain 18% and 11% of the total variance, respectively. EOF-1 represents a north–south dipole pattern, characteristic of the ENSO-induced PJ pattern (Fig. 4b), while in EOF-2 the precipitation anomalies decrease over the KOE and increase over the Sea of Okhotsk. These results are different from those of Kosaka et al. (2011), who focused on early and late summer. Decreased precipitation is also seen over northern China and East Asia, where the EASM circulation and precipitation have weakened during the number of decades (Zhang and Zhou 2015).

Figure 4d shows precipitation regressed on the July KOE SST index (Fig. 3a). It appears that precipitation anomalies eastward of 130°E consist of both the ENSO-induced dipole pattern (EOF-1) and the north–south
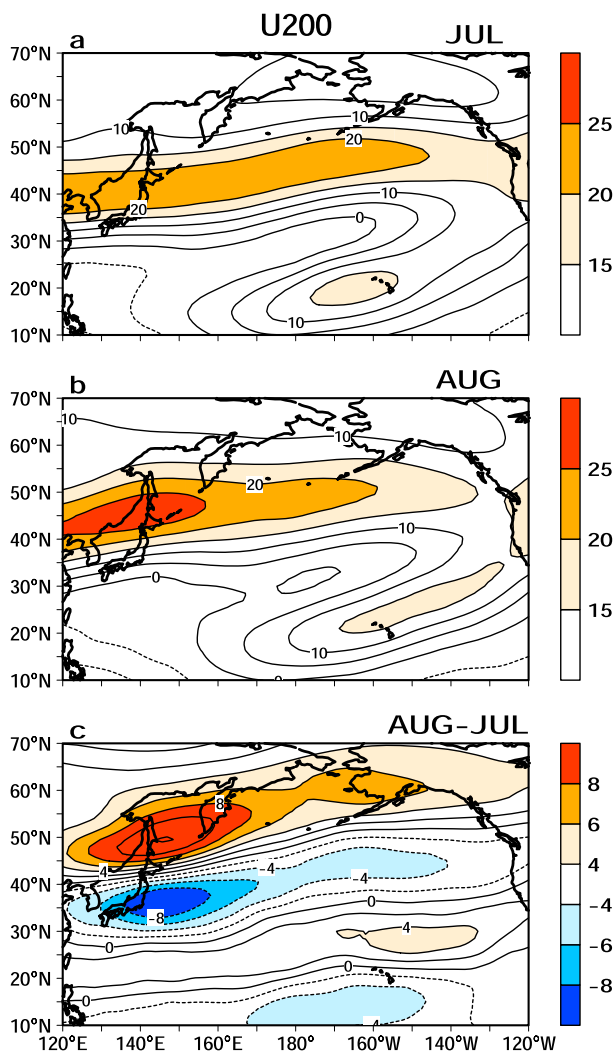
FIG. 5. Climatological zonal wind at 200 hPa in (a) July, (b) August, and (c) August–July difference for the period 1982–2012. Contour interval is 5 m s^{-1} in (a) and (b), and 2 m s^{-1} in (c). Positive values are indicated by solid contours, negative values are indicated by dashed contours.

dipole pattern over the KOE (EOF-2), forming a meridional tripolar pattern that closely resembles that seen in the long-term changes (Matsumura et al. 2015a). Figure 4d suggests that the meridional tripolar pattern is associated with both the ENSO-induced PJ pattern and the KOE SST. Although the PJ pattern is seen throughout the summer (e.g., Wakabayashi and Kawamura 2004), precipitation anomalies regressed on the August KOE SST index vanish in August after the baiu termination (not shown).

b. Atmospheric variability

To understand the precipitation dipole over the KOE in EOF-2, we now focus on July during the baiu season

and August after the baiu season. Figures 5a and 5b show climatological zonal wind at 200 hPa in July and August, respectively. In July, the subtropical jet is located along 40°N, while in August it shifts northward to 45°N. The zonal wind difference between August and July indicates the northward shift of the subtropical jet around Japan and the NW Pacific (Fig. 5c), corresponding closely to a response to the SST frontal shift (Nakamura and Miyama 2014). Consequently, seasonal changes in the NW Pacific SST with a strong SST front play a substantial role in creating the difference in the climatological subtropical jet between August and July. This relation can be also applied to the interannual variability, because the variance in the subtropical jet over the NW Pacific is quantitatively similar to the difference in the climatological jet between August and July (e.g., Lu 2004). Figures 6a and 6c show 200-hPa zonal wind and wind anomalies regressed on the precipitation PC-1 and PC-2 in July. For EOF-1, zonal wind anomalies are zonally uniform, reflecting the ENSO-induced PJ pattern (Fig. 6b), while for EOF-2, positive anomalies are pronounced over the Sea of Okhotsk as a result of a northward shift or a meandering of the subtropical jet, forming an anticyclonic circulation over the KOE. Zonal wind anomalies regressed on the KOE SST index also increase over the Sea of Okhotsk as a result of a northward shift of the subtropical jet, forming an anticyclonic circulation over the KOE (Fig. 6d). The wind anomalies are also zonally uniform like EOF-1, especially in lower latitudes.

In July the climatological subtropical jet is zonally uniform along 40°N (Fig. 5a), whereas in August it is strongest around Japan (Fig. 5b), forming a jet exit. For both the ENSO and KOE SST indices, zonal wind anomalies are also enhanced over the eastern North Pacific in July, but in August they are restricted to the NW Pacific (Figs. 7a and 7b), reflecting the difference in the climatological jet between July and August. Although subtropical precipitation variance is highest in late summer, the ENSO-induced precipitation dipole vanishes in September (Fig. 1b), when ENSO-induced KOE SST anomalies are most significant (Figs. 1a and 2d). Corresponding to the decayed precipitation dipole, ENSO-induced zonal wind anomalies also markedly weaken in September (Fig. 7c), but the northward shift of the subtropical jet associated with the September KOE SST is maintained over the NW Pacific (Fig. 7d), although atmospheric forcing also leads to the KOE SST anomalies. The northward shift of the subtropical jet associated with KOE SST during the summertime is similar to idealized experimental results (Nakamura and Miyama 2014).
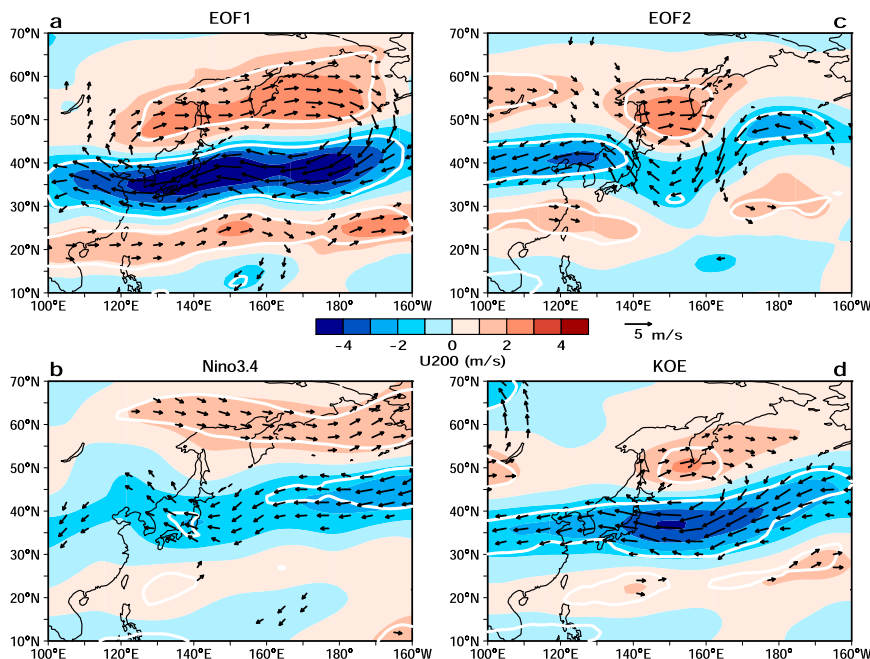
FIG. 6. As in Fig. 4, but for zonal wind (shadings; m s^{-1}) and wind (vectors) anomalies at 200 hPa. White contours indicate statistical significance at the 95% level.

Precipitation EOF-1 represents the ENSO-induced PJ pattern. What then is the physical mechanism of the precipitation EOF-2? Figure 8 shows the 500-hPa geopotential height and SLP anomalies regressed on the precipitation PC-2. Corresponding to a northward shift or a meandering of the subtropical jet, anticyclonic anomalies are located over the KOE and cyclonic anomalies are located over northeastern Siberia. SLP anomalies
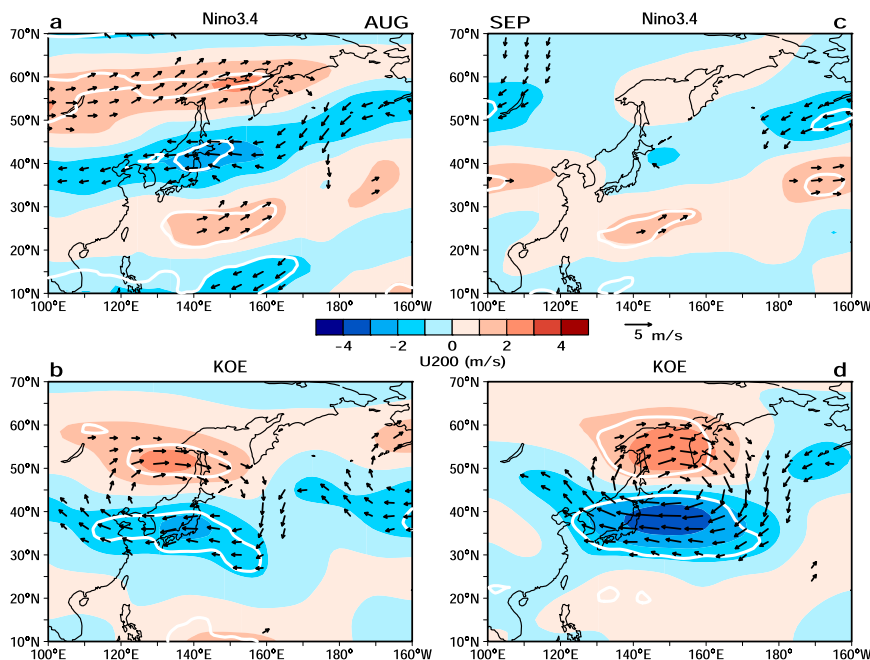

FIG. 7. As in Fig. 6, but for (a),(b) August and (c),(d) September in the preceding NDJ Niño-3.4 SST and KOE SST indices, respectively.
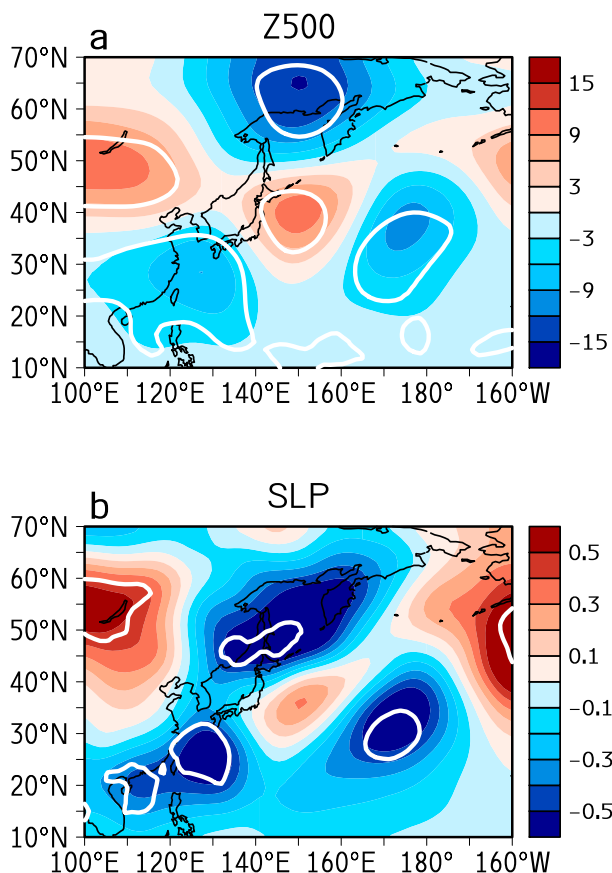
FIG. 8. (a) Geopotential height anomalies (m) at 500 hPa and (b) sea level pressure (hPa) regressed on PC-2. White contours indicate statistical significance at the 95% level.

increase slightly over the KOE, but decrease markedly northeastward over the Sea of Okhotsk. These geopotential height anomalies exhibit a northward tilt with height over the KOE, reflecting a baroclinic response to the northward-shifted baiu rainfall. To the west and east of the anticyclonic anomalies, both cyclonic anomalies exhibit a nearly equivalent barotropic structure. Figure 8 resembles quite well the interannual variation of the Okhotsk high (Figs. 3 and 4 of Tachibana et al. 2004), which is related to the land–sea thermal contrast between warm northeastern Siberia and the cold KOE. Thus, the northward-shifted baiu rainband over the KOE results in decreased SLP over the Sea of Okhotsk, weakening the Okhotsk high. Stationary Rossby waves from Europe also propagate eastward along the Arctic coast and accumulate over northeastern Siberia, affecting the Okhotsk high, but not the anticyclonic anomalies over the KOE (Tachibana et al. 2004). Another strong anticyclonic anomaly is located over southern Siberia around Lake Baikal. This anticyclonic anomaly is quite similar to that

described by Zhu et al. (2012), who demonstrated that surface warming over southern Siberia leads to an anomalous low-level anticyclone, which in turn results in weakened southwesterly EASM winds and a drier climate over northern East Asia. Our precipitation EOF-2 also clearly decreases over northern East Asia (Fig. 4c).

Figure 9 compares vertical sections of diabatic heating and geopotential height anomalies over the NW Pacific (140°–160°E) associated with ENSO, EOF-2, and KOE SST. The ENSO-induced PJ pattern intensifies to anticyclonic anomalies over the KOE, especially in the lower and midtroposphere, forming a precipitation dipole. In the precipitation EOF-2, northward-shifted and enhanced baiu heating leads to stronger upward motion in conjunction with lower-level convergence and upper-tropospheric divergence. As a result, anticyclonic anomalies intensify in the upper troposphere and cyclonic anomalies intensify in the lower troposphere, enhancing the baroclinic structure. To the south of the enhanced baiu heating, enhanced diabatic cooling associated with the downward motion also intensifies the anticyclonic anomalies over the KOE. Diabatic heating anomalies associated with the KOE SST index consist of both the ENSO-induced PJ pattern and the northward-shifted baiu heating over the KOE, forming a tripolar pattern (Fig. 9e). Geopotential height anomalies also reflect both the PJ pattern and northward-shifted baiu heating (Fig. 9f). In addition to KOE SST variability, the northward-shifted baiu heating also appears to accelerate the upper-tropospheric westerlies north of 50°N through Coriolis acceleration of the meridional ageostrophic circulation (Lu and Lin 2009; Sampe and Xie 2010). We therefore suggest that the combination of the PJ pattern, KOE SST, and baiu heating intensifies the anticyclonic anomalies with a baroclinic structure.

As noted earlier, KOE SST variance in summer is much larger than its anomalies associated with the ENSO-induced PJ pattern (Fig. 1a). Thus, the KOE SST variations may be driven by not only the PJ pattern but also other atmospheric forcings, such as the Silk Road pattern (Enomoto et al. 2003; Enomoto 2004) that can affect the KOE SST variations through the WPSH. We therefore present the following hypotheses. 1) Atmospheric forcings, such as the ENSO-induced PJ pattern, increase KOE SST. 2) The increased KOE SST enhances northward shifts in the subtropical jet and baiu rainband, leading to 3) weakening of the Okhotsk high and anticyclonic anomalies over the KOE. 4) The intensified anticyclone further increases the KOE SST. Indeed, corresponding to the intensified anticyclonic anomalies
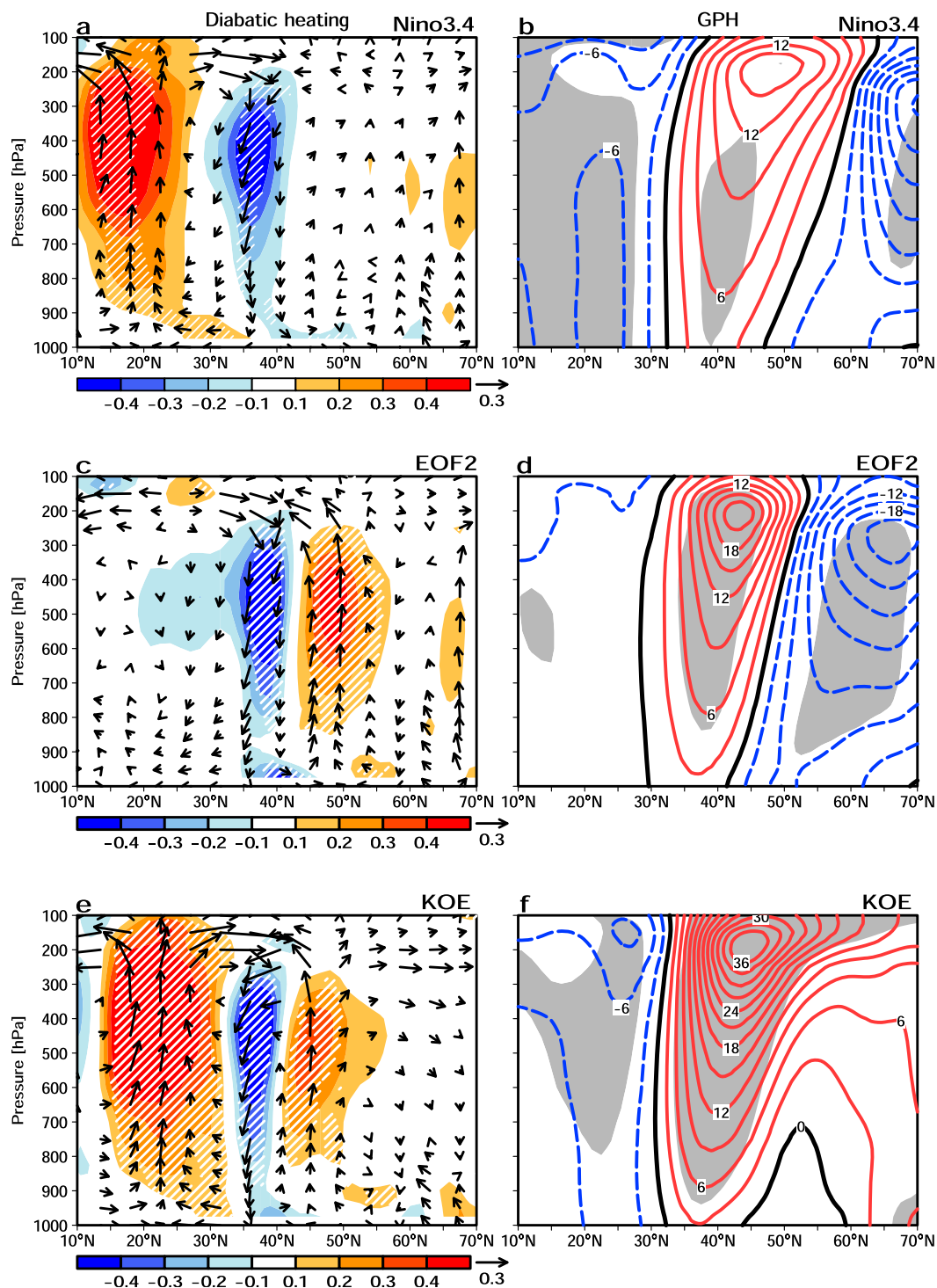
FIG. 9. Meridional sections of diabatic heating (K day^{-1}) and meridional circulation (vectors, m s^{-1}) averaged over 140°–160°E regressed on (a) the preceding NDJ Niño-3.4 SST index, (c) PC-2, and (e) KOE SST index. Hatched regions indicate statistical significance at the 95% level. (b),(d),(f) As in (a),(c),(e), but for geopotential height (3-m contour interval). Shaded regions indicate statistical significance at the 95% level. Thick black solid contours indicate 0 m; positive values are indicated by solid red contours, and negative values are indicated by dashed blue contours.

over the KOE (Fig. 8), KOE SST anomalies regressed onto the precipitation PC-2 increase in July and even in August (not shown), suggesting that the July atmospheric forcing enhances the SST anomalies. Since the influence of the ENSO-induced PJ pattern on KOE SST is robust, as seen in previous studies and Fig. 2, we performed model experiments to clarify processes 2 and 3, as described in the following section.

4. Model experiments

The model domain focuses on the NW Pacific poleward of 30°N to exclude the PJ pattern induced by subtropical convective forcing. The total precipitation in the CTRL run averaged for the period 1982–2012 reproduces well the baiu rainband over the NW Pacific seen in the observations (not shown). The CTRL–NOMP difference provides the atmospheric response derived from baiu heating by the cloud microphysics scheme. Similarly, the CTRL–CLIM difference provides the atmospheric response derived from the SST forcing. The diabatic heating difference between the CTRL and NOMP runs averaged for the period 1982–2012 shows a maximum in the upper troposphere, reflecting condensational heating differences. During the baiu season, cumulus precipitation dominates over the southern part of the KOE, whereas grid-scale precipitation produced by the cloud microphysics scheme dominates the northern part of the KOE in our model experiments. In June, the grid-scale precipitation is much greater than the cumulus precipitation over the KOE, but they are closer in July. The diabatic heating difference between the CTRL and NOMP runs performs well in reflecting the baiu rainfall over the NW Pacific (not shown).

a. Subtropical jet and precipitation responses

Figure 10 compares 200-hPa zonal wind regressed on the KOE SST index in July and August. Note that the color scales are different for the CTRL run and its differences. In July, the observed northward shift of the subtropical jet (Fig. 6d) is well reproduced in the CTRL run and the CTRL–NOMP difference, where the anomalies explain roughly 50% of those in the CTRL run. This result demonstrates that the zonal wind anomalies associated with the variability of the KOE SST are enhanced by diabatic processes associated with baiu heating, which accelerates the westerlies to its north and decelerates the westerlies to its south. The northward shift of the subtropical jet is also robust in the CTRL–CLIM difference, where the anomalies explain 15%–25%

of those in the CTRL run. Consequently, both baiu heating and KOE SST contribute to the northward shift of the subtropical jet in July.

In August, the CTRL run also reproduces well the observed northward shift of the subtropical jet (Fig. 7b) that results in the contrasting north–south anomalies across the climatological jet exit. In the CTRL–NOMP difference, pronounced wind anomalies mostly vanish, because August is the season when the baiu rainband disappears and cumulus precipitation tends to become stronger. However, the CTRL–CLIM difference captures the contrasting north–south wind anomalies, which explain 20–30% of those in the CTRL run, indicating that the northward-shifted subtropical jet in August is enhanced by KOE SST variability. Since the baiu rainband is also enhanced by the lower-tropospheric southwesterlies along the western ridge of the WPSH, the north–south contrasting wind anomalies extend northeastward in July. However, in August when the baiu rainband disappears, the wind anomalies are zonally symmetric across 45°N, reflecting only the KOE SST variability.

Figure 11 shows grid-scale and cumulus precipitation anomalies in July. Grid-scale precipitation anomalies in the CTRL run reproduce well the observed northward shift of the baiu rainband (Fig. 4d), while cumulus precipitation anomalies are limited around Japan, indicating that the observed northward shift of the baiu rainband is explained mainly by the changes in grid-scale precipitation in our experiments. We also confirm that total precipitation anomalies in the CTRL run capture well the northward-shifted rainband, similar to the observations. The CTRL–NOMP and CTRL–CLIM differences also capture well the northward shift of the baiu rainband, corresponding to the northward-shifted subtropical jet. Over the southern part of the KOE, however, increased cumulus precipitation anomalies are pronounced in the CTRL–CLIM difference, unlike the CTRL run and the CTRL–NOMP difference. The strong cumulus precipitation anomalies appear to reflect a response to increased KOE SST anomalies, which will be discussed in section 5.

b. Vertical structures

Figure 12 shows vertical structures of diabatic heating and cloud over the NW Pacific (140°–160°E) regressed on the KOE SST index. Corresponding to the northward shift of the baiu rainband, in the upper troposphere, diabatic heating anomalies are enhanced over 50°–55°N and diabatic cooling anomalies are enhanced over 35°–40°N in the CTRL run, resulting in north–south contrasting cloud anomalies that are consistent with the ERA-Interim reanalysis (Figs. 9c and 9e). The
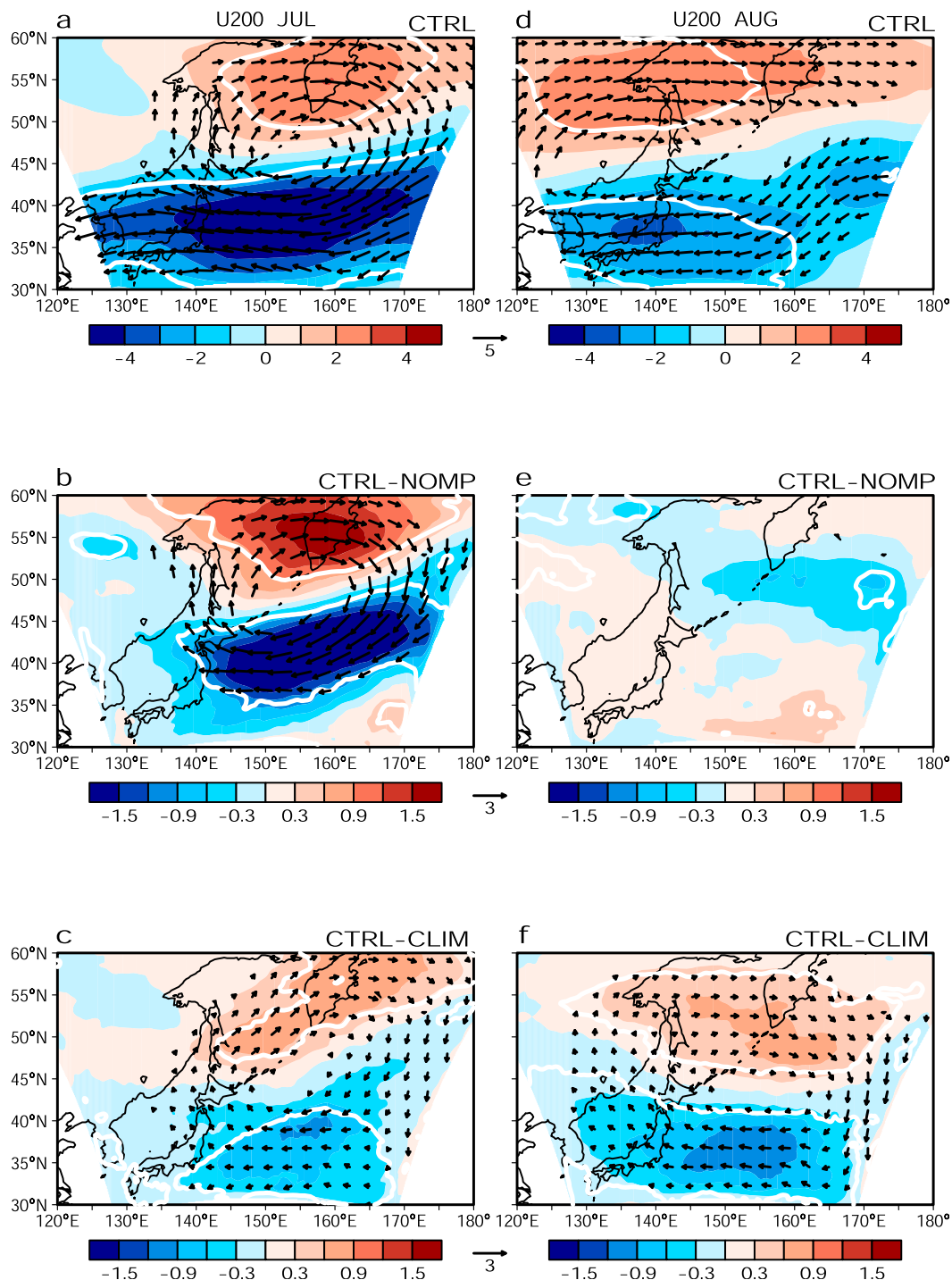
FIG. 10. Zonal wind (shadings; m s^{-1}) and wind (vectors) anomalies at 200 hPa regressed on the KOE SST index in July in (a) the CTRL run, (b) CTRL–NOMP difference, and (c) CTRL–CLIM difference. (d),(e),(f) As in (a),(b),(c), but for August. White contours indicate statistical significance at the 95% level.

north–south contrasting diabatic heating and cloud anomalies are also robust in the CTRL–NOMP difference. In the midtroposphere, however, diabatic cooling anomalies are enhanced over the Sea of

Okhotsk around 45°–50°N in both the CTRL and CTRL–NOMP difference. On the other hand, low clouds and sea fog are increased by surface condensation due to southwesterlies along the WPSH across
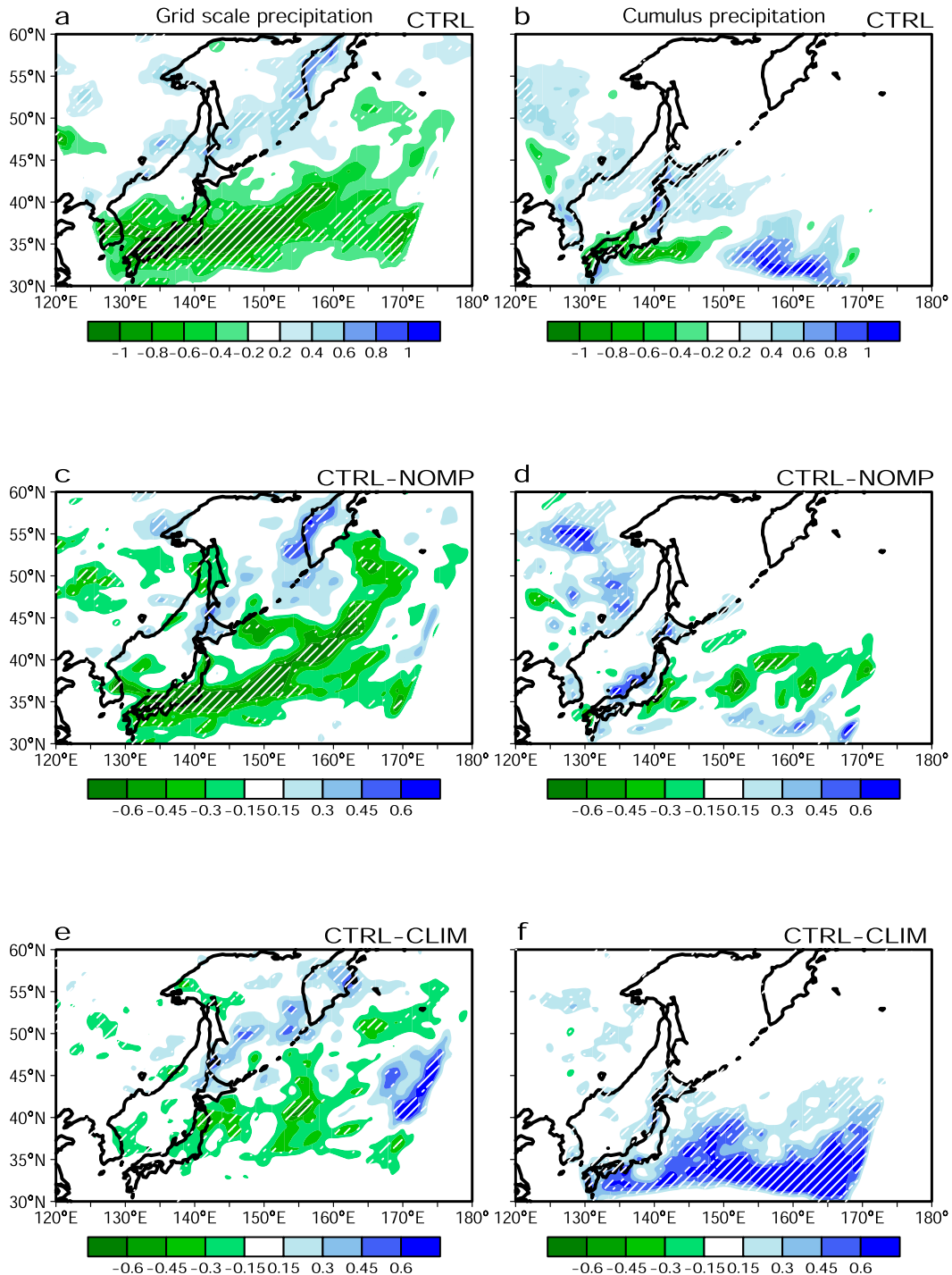
FIG. 11. As in Fig. 10, but for (a),(c),(e) grid-scale precipitation and (b),(d),(f) cumulus precipitation (mm day^{-1}) in July. Hatched regions indicate statistical significance at the 95% level.

the KOE SST front and also by cool SST in the Sea of Okhotsk (Tokinaga and Xie 2009), where a strong surface inversion layer forms. As a result of the increased low clouds, the midtropospheric diabatic cooling is enhanced presumably because of radiative

cooling from the cloud top. These results suggest that enhanced midtropospheric diabatic cooling weakens the northward-shifted baiu heating. Indeed, in the CTRL–NOMP difference, northward-shifted cloud anomalies around 45°–50°N decrease in the mid

FIG. 12. Meridional sections of diabatic heating in July averaged over 140°–160°E regressed on the July KOE SST index in (a) the CTRL run, (c) CTRL–NOMP difference, and (e) CTRL–CLIM difference. Hatched regions indicate statistical significance at the 95% level. (b),(d),(f) As in (a),(c),(e), but for cloud water mixing ratio (cloud water + rainwater + ice + snow + graupel: $10^{-2}\,\mathrm{g\,kg^{-1}}$). Shaded regions indicate statistical significance at the 95% level. The zero contour is omitted; positive values are indicated by solid red contours, and negative values are indicated by dashed blue contours.

troposphere, where there are no significant anomalies in the CTRL run. However, the enhanced midtropospheric diabatic cooling is not found in the ERA-Interim reanalysis (Fig. 9e). This difference might be responsible for the longstanding problem of representing marine boundary layer clouds in global climate models (e.g., Teixeira and Hogan 2002).

Although diabatic heating in the CTRL–CLIM difference (Fig. 12e) does not capture the north–south contrasting anomalies well, the north–south contrast is clearly seen in cloud anomalies (Fig. 12f), corresponding to the grid-scale precipitation anomalies (Fig. 11e). Low clouds also increase over 50°N, but significantly decrease over the KOE. When the KOE SST index is positive, the KOE SST in the CLIM run is lower than in the CTRL run. Thus, in the CLIM run lower-level southwesterlies along the WPSH suppress surface evaporation and increase low cloud across the KOE SST front, causing negative low cloud anomalies.

Figures 13a and 13b show temperature and geopotential height for the CTRL run, respectively, which reproduce the observed geopotential height anomalies (Fig. 9f); the anticyclonic anomalies exhibit a northward tilt with height. The CTRL–NOMP difference enhances the baroclinic atmospheric circulation (Figs. 13c and 13d). The northward-shifted baiu heating (Fig. 12c) accounts for the upper-tropospheric warming anomalies, while those in the lower troposphere (1000–700 hPa) are caused by southwesterly-induced warm advection (not shown). As a result of the enhanced baiu heating, the upper-tropospheric ridge intensifies over 45°–50°N, and the lower-level anticyclonic anomalies intensify over the KOE around 35°–40°N by enhancing diabatic cooling (Fig. 12c). Over the Sea of Okhotsk north of 50°N, lower-level geopotential height decreases, although the negative height anomalies are quite small presumably because of enhanced diabatic cooling due to increased low cloud (Figs. 12c and 12d). The CTRL–CLIM difference also enhances the baroclinic atmospheric circulation (Figs. 13e and 13f). In the upper troposphere, increased temperature anomalies are consistent with the fact that horizontal advection there has a warming tendency, while the lower-tropospheric anomalies appear to be caused by surface heat flux over the KOE (Fig. 12e). In the lower layer, cyclonic anomalies are much stronger than those in the CTRL run because of a response to KOE SST variability.

In August, when the baroclinic forcing weakens, pronounced anomalies mostly vanish in the CTRL–NOMP difference (Figs. 14c and 14d), consistent with simulated subtropical jet responses (Fig. 10e). In the CTRL–CLIM difference (Figs. 14e and 14f), anticyclonic anomalies are located over 35°–45°N and cyclonic anomalies north of 45°N, forming an equivalent barotropic-like structure. The north–south contrasting barotropic-like response explains 30%–50% of the anomalies in the CTRL run (Figs. 14a and 14b), which results from the KOE SST variability through the northward shift of the subtropical jet (Fig. 10f), suggesting the importance of the KOE SST feedback. In conclusion, in July both baiu heating and KOE SST cause the baroclinic intensification of anticyclonic circulation while in August the KOE SST causes the barotropic-like intensification of anticyclonic circulation.

c. JJA SLP response

As shown above, the atmospheric variability in July is greater than in August because baiu forcing amplifies the atmospheric circulation. In June when the baiu season begins, however, ENSO-induced SST anomalies are not pronounced in the KOE (Fig. 2a) and the atmospheric responses to KOE SST anomalies are not robust (not shown). Idealized model experiments also demonstrate that the atmospheric response to the NW Pacific SST anomalies is weak in June, but strong in July and August (Nakamura and Miyama 2014), consistent with our results. In the long-term changes, the summer [June–August (JJA)] WPSH has intensified and the Okhotsk high has weakened (Matsumura et al. 2015a). We now examine the north–south contrasting changes between the two highs in the interannual variability.

Figure 15a shows JJA SLP regressed on the JJA KOE SST index in the CTRL run. Negative (positive) SLP anomalies are located over the Sea of Okhotsk (NW Pacific), resulting in contrasting north–south anomalies across 40°N, which resemble recent changes in the WPSH and Okhotsk high. The CTRL–NOMP difference (Fig. 15b) also intensifies over the NW Pacific due to enhanced diabatic cooling as a result of the northward-shifted baiu heating in July. However, negative SLP anomalies over the Sea of Okhotsk are weaker than those in the CTRL run, likely reflecting enhanced midtropospheric diabatic cooling due to increased low cloud (Figs. 12c and 12d). Since in the CTRL–CLIM difference cyclonic anomalies are strong in the lower layer (Figs. 13f and 14f), we show 500-hPa geopotential height anomalies instead of SLP. In the CTRL run (Fig. 15c), positive height anomalies intensify northward compared with the SLP anomalies. The CTRL–CLIM difference (Fig. 15d) strengthens the contrasting north–south height anomalies by shifting the subtropical jet northward. As a result, both baiu heating and KOE SST intensify the cyclonic anomalies around the Sea of Okhotsk and anticyclonic anomalies over the NW
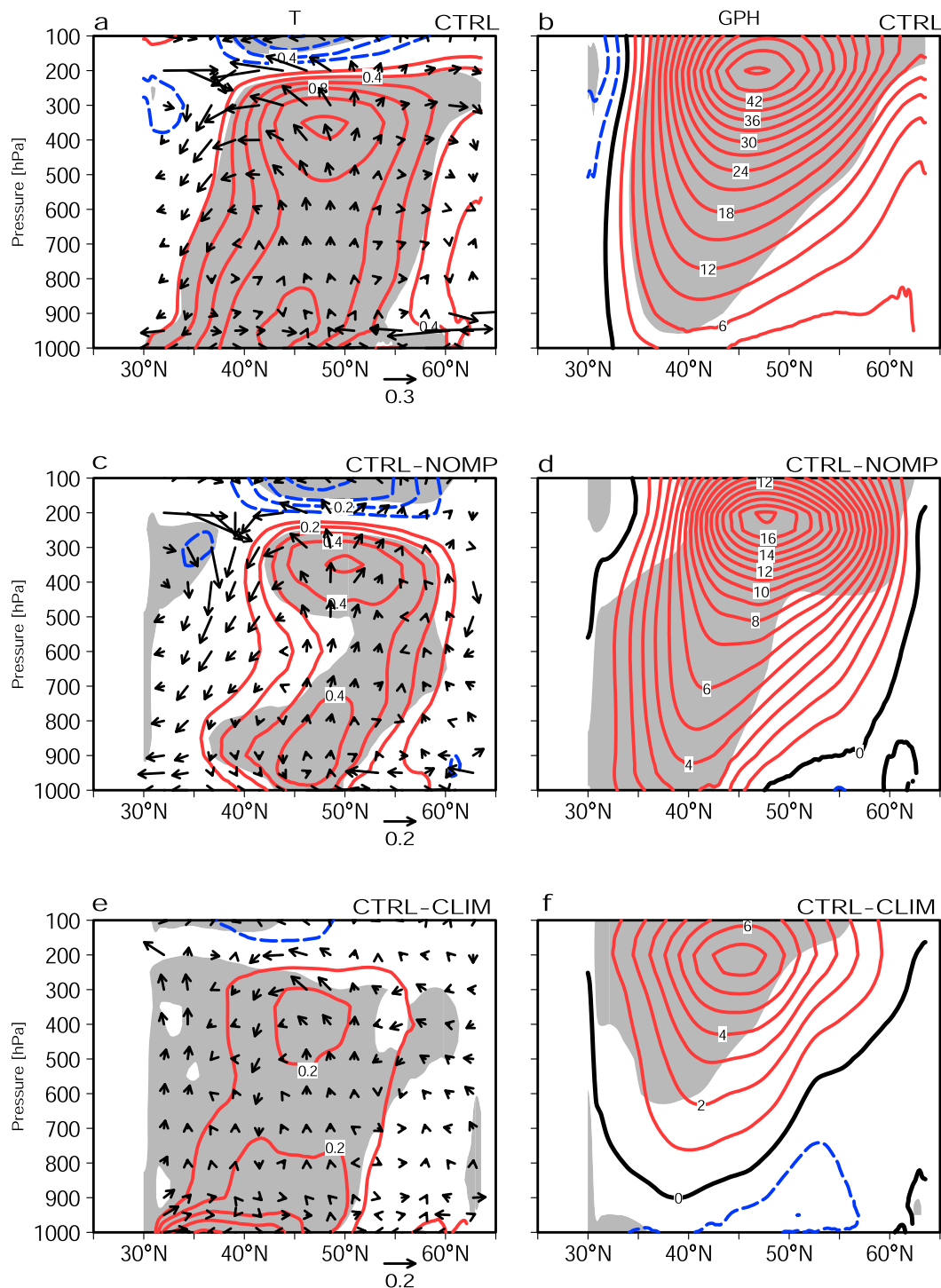
FIG. 13. As in Fig. 12, but for (a),(c),(e) temperature (contour interval: (a) 0.2 K and (c),(e) 0.1 K) and meridional circulation (vectors, m s^{-1}); and (b),(d),(f) geopotential height (contour interval: (b) 2 m and (d),(f) 1 m). Thick black solid contours indicate 0 m.

Pacific during JJA. These results are similar to the second EOF of Arai and Kimoto (2008), who simulated the first (PJ pattern) and second (north–south dipole) EOF modes of 500-hPa geopotential height in an ensemble atmospheric model experiment. Our model results therefore suggest that as with the PJ pattern, baiu heating and KOE SST can amplify the summer WPSH in its interannual variability.
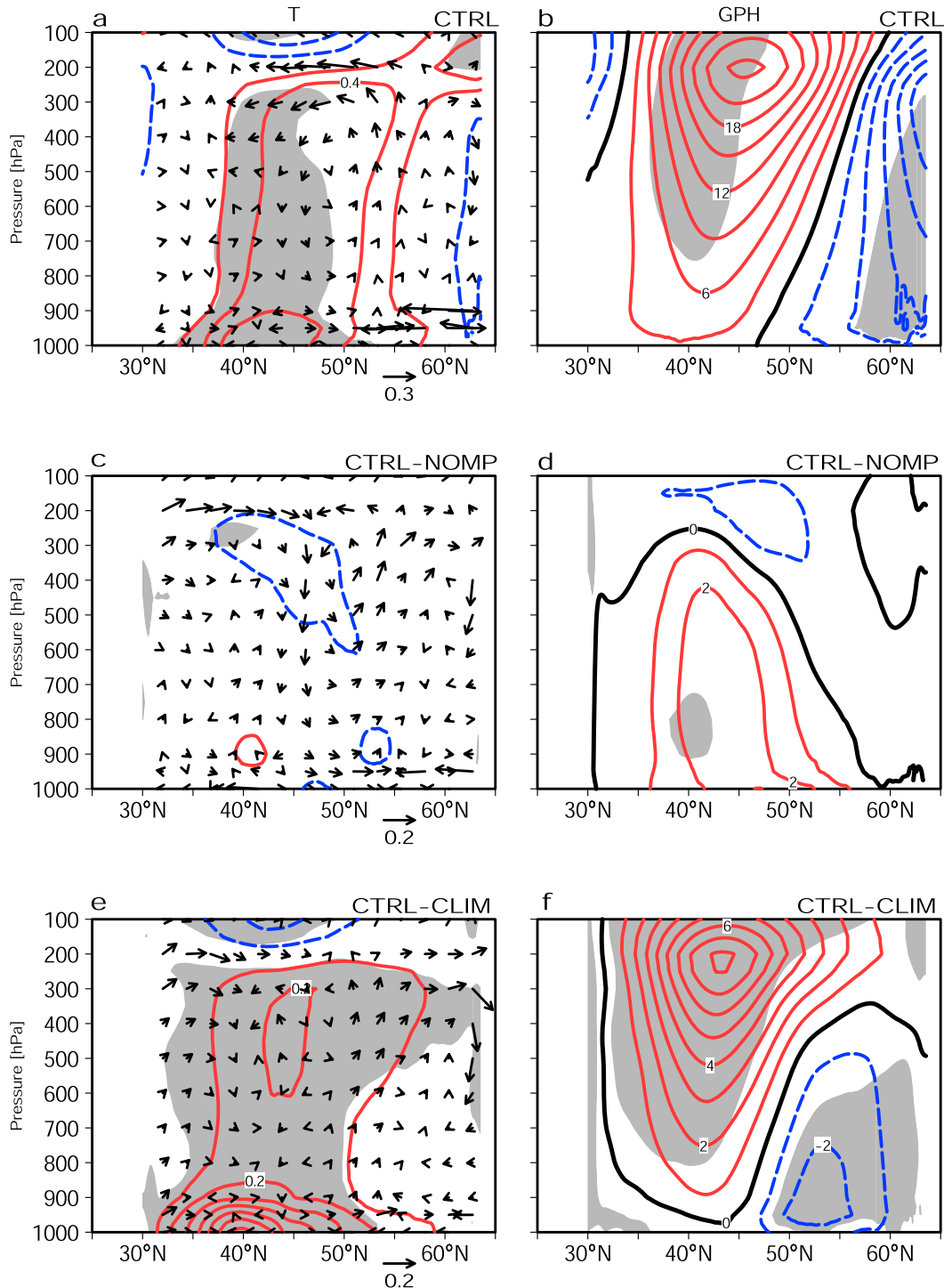
FIG. 14. As in Fig. 13, but for August.

5. Summary and discussion

We investigated the response of the interannual variability of baiu rainfall to KOE SST anomalies and its impact on atmospheric circulation for the period 1982–2012 using observations and a regional climate model. In July, the precipitation EOF-1 represents the meridional dipole between subtropical and baiu rainfall, while EOF-2 features the northward-shifted baiu rainband over the KOE, suggesting that the ENSO-induced precipitation dipole and the northward-shifted baiu rainfall
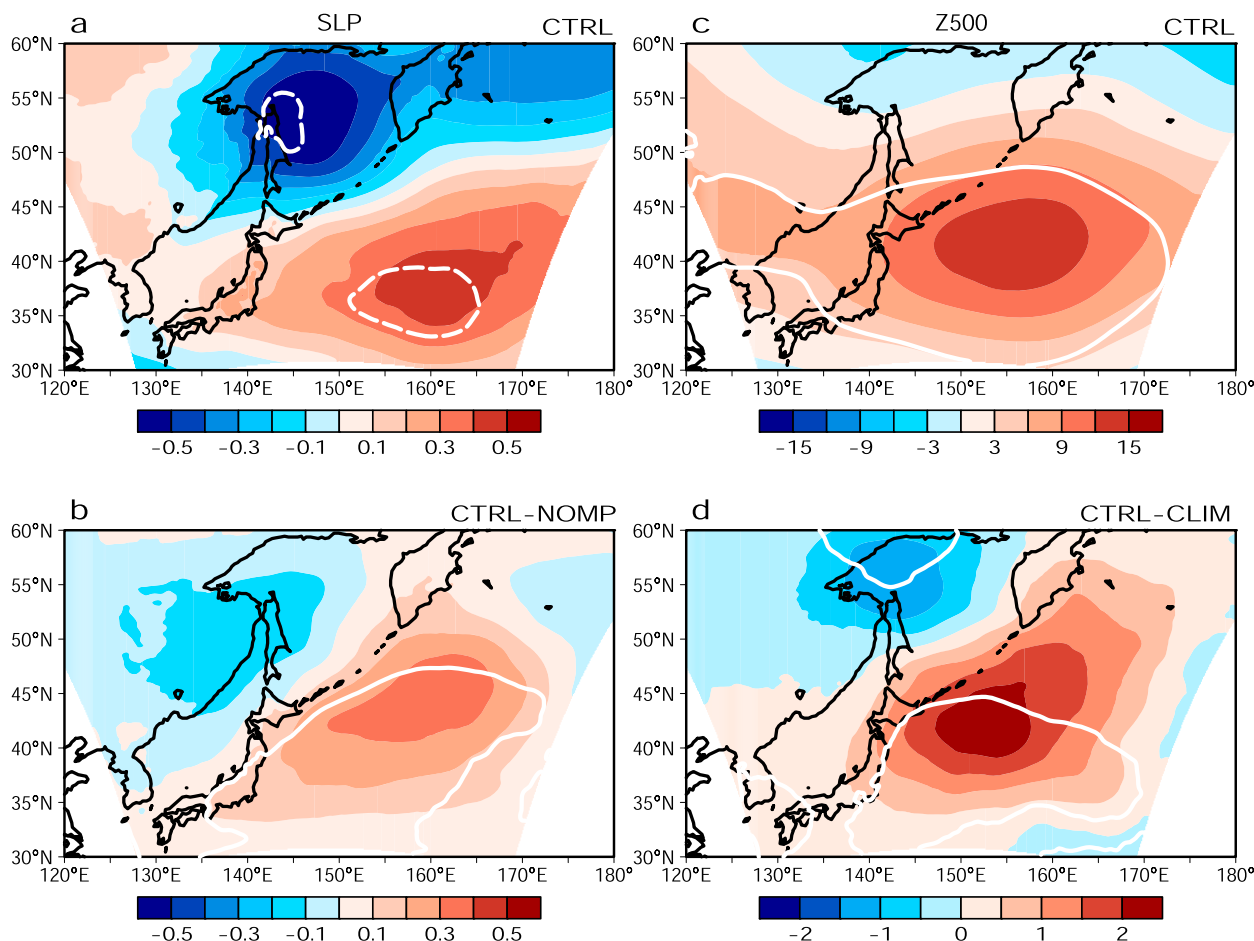
FIG. 15. JJA SLP (hPa) regressed on the JJA KOE SST index in (a) the CTRL run and (b) CTRL–NOMP difference. (c),(d) As in (a),(b), but for 500-hPa geopotential height (m) in (c) the CTRL run and (d) CTRL–CLIM difference. White solid (dashed) contours indicate statistical significance at the 95% (90%) level.

are independent of each other. Although the ENSO-induced PJ pattern leads to the meridional precipitation dipole during the summer, increased KOE SST in July shifts the baiu rainfall northward with the subtropical jet, forming a tripolar precipitation pattern. Our main results can be summarized as follows: 1) atmospheric forcings, such as the ENSO-induced PJ pattern, increase KOE SST; 2) the increased KOE SST enhances northward shifts in the subtropical jet and baiu rainband, leading to 3) weakening of the Okhotsk high and anticyclonic anomalies over the KOE; and 4) the intensified anticyclone can further increase the KOE SST. Consequently, it is important to consider air–sea interaction over the KOE to gain a better understanding of the summer NW Pacific climate.

During summer both increased KOE SST and enhanced baiu heating contribute to the cyclonic anomalies over the Sea of Okhotsk and anticyclonic anomalies over the NW Pacific. This result indicates that the recent

northward-shifted trend of baiu rainfall might also be induced by KOE SST warming, leading to the north–south contrasting changes between the weakened Okhotsk high and intensified WPSH (Matsumura et al. 2015a). Although in the long-term changes, the north–south contrast between the Okhotsk high and WPSH is robust, in the interannual variability the correlation between the two highs is quite weak because many different factors may drive the variability of the WPSH and Okhotsk high (e.g., Nitta 1987; Enomoto et al. 2003; Matsumura et al. 2015b). In addition, while baiu heating is not shifted northward to the Sea of Okhotsk in the long-term changes, it is shifted there in the interannual variability. As a result, over the Sea of Okhotsk, increased low cloud enhances radiative cooling from the low cloud top (Fig. 12), weakening the northward-shifted baiu heating and the resultant SLP anomalies, which also results in a weak relation between the WPSH and Okhotsk high in the interannual variability. However,

the enhanced midtropospheric diabatic cooling is not found in the ERA-Interim reanalysis (Fig. 9e). Since current global climate models show large diversity in the representation of the EASM/baiu rainband (e.g., Ninomiya 2009), it is possible that a better simulation of baiu-rainband activity in global climate models requires further improvements in the representation of low clouds.

A regional climate model can simulate baiu-rainband activity better than global climate models, but our model experiments do not completely reproduce the baiu rainfall variability. Observed precipitation anomalies over northern China are not significant (Fig. 3d), while simulated cumulus precipitation anomalies increase in all of the experiments (Fig. 11), indicating that cumulus precipitation may be too strong. In particular, strong cumulus precipitation anomalies are seen over the southern part of the KOE in the CTRL–CLIM difference (Fig. 11f), even in June and August. It is possible that the observed SST anomalies are overestimated in our model experiments, especially in summer when atmospheric forcing can be the primary drivers of the KOE SST anomalies. As a result, increased cumulus convective heating (Fig. 12e) can enhance a baroclinic structure over the southern part of the KOE (e.g., Fig. 13f), where upward motion is enhanced (Fig. 13e), while in the CTRL and CTRL–NOMP difference, downward motion is enhanced (Figs. 13a,c), possibly suggesting that process 4 leads to the overestimated KOE SST anomalies in our experiments. Using an atmosphere–ocean coupled model may help improve representation of the cumulus precipitation over the KOE.

In the present study the polarity of the ENSO index is reversed to emphasize positive KOE SST anomalies induced by La Niña. Thus, our results can also be summarized as follows when the ENSO index is in a positive phase. The El Niño–induced PJ pattern results in enhanced baiu rainfall and reduced KOE SST, which in turn enhances the southward shift of the subtropical jet, leading to strengthening of the Okhotsk high and cyclonic anomalies over the KOE. However, since there is an asymmetry in the duration of El Niño and La Niña (Okumura and Deser 2010), the influence of this asymmetry on the NW Pacific summer climate variability needs further investigation. In addition to the ENSO-induced KOE SST, the PDO may also play an important role in the summer NW Pacific and East Asian climate (e.g., Feng et al. 2014). Both the interannual and decadal time scales of the PDO are related to ENSO, but there are also independent signals whose variability is concentrated mainly along the KOE (e.g., Kwon et al. 2010). The PDO is regarded as one of the possible factors that have weakened the EASM over northern East Asia (Li et al. 2010). Although the ENSO-induced PJ pattern is the main driver of the NW Pacific climate variability, we must consider the NW Pacific SST as well as tropical oceans to better understand the East Asian summer climate.

REFERENCES

Arai, M., and M. Kimoto, 2008: Simulated interannual variation in summertime atmospheric circulation associated with the East Asian monsoon. *Climate Dyn.*, **31**, 435–447, doi:10.1007/s00382-007-0317-y.

Chowdary, J. S., S.-P. Xie, J.-J. Luo, J. Hafner, S. Behera, Y. Masumoto, and T. Yamagata, 2011: Predictability of Northwest Pacific climate during summer and the role of the tropical Indian Ocean. *Climate Dyn.*, **36**, 607–621, doi:10.1007/s00382-009-0686-5.

Dee, D. P., and Coauthors, 2011: The ERA-Interim reanalysis: Configuration and performance of the data assimilation system. *Quart. J. Roy. Meteor. Soc.*, **137**, 553–597, doi:10.1002/qj.828.

Enomoto, T., 2004: Interannual variability of the Bonin high associated with the propagation of Rossby waves along the Asian jet. *J. Meteor. Soc. Japan*, **82**, 1019–1034, doi:10.2151/jmsj.2004.1019.

——, B. J. Hoskins, and Y. Matsuda, 2003: The formation mechanism of the Bonin high in August. *Quart. J. Roy. Meteor. Soc.*, **129**, 157–178, doi:10.1256/qj.01.211.

Feng, J., L. Wang, and W. Chen, 2014: How does the East Asian summer monsoon behave in the decaying phase of El Niño during different PDO phases? *J. Climate*, **27**, 2682–2698, doi:10.1175/JCLI-D-13-00015.1.

Frankignoul, C., and N. Sennechael, 2007: Observed influence of North Pacific SST anomalies on the atmospheric circulation. *J. Climate*, **20**, 592–606, doi:10.1175/JCLI4021.1.

——, ——, Y.-O. Kwon, and M. A. Alexander, 2011: Influence of the meridional shifts of the Kuroshio and the Oyashio extensions on the atmospheric circulation. *J. Climate*, **24**, 762–777, doi:10.1175/2010JCLI3731.1.

Grell, G. A., and D. Dévényi, 2002: A generalized approach to parameterizing convection combining ensemble and data assimilation techniques. *Geophys. Res. Lett.*, **29**, doi:10.1029/2002GL015311.

Hirota, N., and M. Takahashi, 2012: A tripolar pattern as an internal mode of the East Asian summer monsoon. *Climate Dyn.*, **39**, 2219–2238, doi:10.1007/s00382-012-1416-y.

Hong, S. Y., J. Dudhia, and S. H. Chen, 2004: A revised approach to ice microphysical processes for the bulk parameterization of clouds and precipitation. *Mon. Wea. Rev.*, **132**, 103–120, doi:10.1175/1520-0493(2004)132<0103:ARATIM>2.0.CO;2.

Huang, G., K. Hu, and S.-P. Xie, 2010: Strengthening of tropical Indian Ocean teleconnection to the Northwest Pacific since the mid-1970s: An atmospheric GCM study. *J. Climate*, **23**, 5294–5304, doi:10.1175/2010JCLI3577.1.

Huffman, G. J., and Coauthors, 1997: The Global Precipitation Climatology Project (GPCP) combined precipitation

dataset. *Bull. Amer. Meteor. Soc.*, **78**, 5–20, doi:10.1175/1520-0477(1997)078<0005:TGPCPG>2.0.CO;2.

Kosaka, Y., S.-P. Xie, and H. Nakamura, 2011: Dynamics of interannual variability in summer precipitation over East Asia. *J. Climate*, **24**, 5435–5453, doi:10.1175/2011JCLI4099.1.

——, J. S. Chowdary, S.-P. Xie, Y.-M. Min, and J.-Y. Lee, 2012: Limitations of seasonal predictability for summer climate over East Asia and the northwestern Pacific. *J. Climate*, **25**, 7574–7589, doi:10.1175/JCLI-D-12-00009.1.

Kurihara, K., and T. Tsuyuki, 1987: Development of the barotropic high around Japan and its association with Rossby wave-like propagations over the North Pacific: Analysis of August 1984. *J. Meteor. Soc. Japan*, **65**, 237–246.

Kwon, Y.-O., M. A. Alexander, N. A. Bond, C. Frankignoul, H. Nakamura, B. Qiu, and L. A. Thompson, 2010: Role of the Gulf Stream and Kuroshio–Oyashio systems in large-scale atmosphere–ocean interaction: A review. *J. Climate*, **23**, 3249–3281, doi:10.1175/2010JCLI3343.1.

Li, H., A. Dai, T. Zhou, and J. Lu, 2010: Responses of East Asian summer monsoon to historical SST and atmospheric forcing during 1950–2000. *Climate Dyn.*, **34**, 501–514, doi:10.1007/s00382-008-0482-7.

Lu, R., 2004: Associations among the components of the East Asian summer monsoon system in the meridional direction. *J. Meteor. Soc. Japan*, **82**, 155–165, doi:10.2151/jmsj.82.155.

——, and Z. Lin, 2009: Role of subtropical precipitation anomalies in maintaining the summertime meridional teleconnection over the NW Pacific and East Asia. *J. Climate*, **22**, 2058–2072, doi:10.1175/2008JCLI2444.1.

Mantua, N. J., S. R. Hare, Y. Zhang, J. M. Wallace, and R. Francis, 1997: A Pacific interdecadal climate oscillation with impacts on salmon production. *Bull. Amer. Meteor. Soc.*, **78**, 1069–1079, doi:10.1175/1520-0477(1997)078<1069:APICOW>2.0.CO;2.

Matsumura, S., S. Sugimoto, and T. Sato, 2015a: Recent intensification of the western Pacific subtropical high associated with the East Asian summer monsoon. *J. Climate*, **28**, 2873–2883, doi:10.1175/JCLI-D-14-00569.1.

——, K. Yamazaki, and T. Sato, 2015b: Role of Siberian land-atmosphere coupling in the development of the August Okhotsk High in 2008. *J. Meteor. Soc. Japan*, **93**, 229–244, doi:10.2151/jmsj.2015-013.

Nakamura, M., and S. Yamane, 2010: Dominant anomaly patterns in the near-surface baroclinicity and accompanying anomalies in the atmosphere and oceans. Part II: North Pacific basin. *J. Climate*, **23**, 6445–6467, doi:10.1175/2010JCLI3017.1.

——, and T. Miyama, 2014: Impacts of the Oyashio temperature front on the regional climate. *J. Climate*, **27**, 7861–7873, doi:10.1175/JCLI-D-13-00609.1.

Ninomiya, K., 2009: Characteristics of precipitation in the Meiyu-baiu season in the CMIP3 20th century climate simulations. *J. Meteor. Soc. Japan*, **87**, 829–843, doi:10.2151/jmsj.87.829.

——, T. Nishimura, W. Ohfuchi, T. Suzuki, and S. Matsumura, 2002: Features of the baiu front simulated in an AGCM

(T42L52). *J. Meteor. Soc. Japan*, **80**, 697–716, doi:10.2151/jmsj.80.697.

Nitta, T., 1987: Convective activities in the tropical western Pacific and their impact on the Northern Hemisphere summer circulation. *J. Meteor. Soc. Japan*, **65**, 373–390.

Okumura, Y. M., and C. Deser, 2010: Asymmetry in the duration of El Niño and La Niña. *J. Climate*, **23**, 5826–5843, doi:10.1175/2010JCLI3592.1.

Rayner, N. A., P. Brohan, D. E. Parker, C. K. Folland, J. J. Kennedy, M. Vanicek, T. Ansell, and S. F. B. Tett, 2006: Improved analyses of changes and uncertainties in sea surface temperature measured in situ since the mid-nineteenth century: The HadSST2 dataset. *J. Climate*, **19**, 446–469, doi:10.1175/JCLI3637.1.

Reynolds, R. W., T. M. Smith, C. Liu, D. B. Chelton, K. S. Casey, and M. G. Schlax, 2007: Daily high resolution blended analysis for sea surface temperatures. *J. Climate*, **20**, 5473–5496, doi:10.1175/2007JCLI1824.1.

Sampe, T., and S.-P. Xie, 2010: Large-scale dynamics of the meiyu–baiu rainband: Environmental forcing by the westerly jet. *J. Climate*, **23**, 113–134, doi:10.1175/2009JCLI3128.1.

Skamarock, W. C., and Coauthors, 2008: A description of the Advanced Research WRF version 3. NCAR Tech. Note NCAR/TN-475+STR, 113 pp., doi:10.5065/D68S4MVH.

Tachibana, Y., T. Iwamoto, M. Ogi, and Y. Watanabe, 2004: Abnormal meridional temperature gradient and its relation to the Okhotsk high. *J. Meteor. Soc. Japan*, **82**, 1399–1415, doi:10.2151/jmsj.2004.1399.

Teixeira, J., and T. Hogan, 2002: Boundary layer clouds in a global atmospheric model: Simple cloud cover parameterizations. *J. Climate*, **15**, 1261–1276, doi:10.1175/1520-0442(2002)015<1261:BLCIAG>2.0.CO;2.

Tokinaga, H., and S.-P. Xie, 2009: Ocean tidal cooling effect on summer sea fog over the Okhotsk Sea. *J. Geophys. Res.*, **114**, D14102, doi:10.1029/2008JD011477.

Ueda, H., T. Yasunari, and R. Kawamura, 1995: Abrupt seasonal change of large-scale convective activity over the western Pacific in the northern summer. *J. Meteor. Soc. Japan*, **73**, 795–809.

Wakabayashi, S., and R. Kawamura, 2004: Extraction of major teleconnection patterns possibly associated with the anomalous summer climate in Japan. *J. Meteor. Soc. Japan*, **82**, 1577–1588, doi:10.2151/jmsj.82.1577.

Xie, S.-P., K. Hu, J. Hafner, H. Tokinaga, Y. Du, G. Huang, and T. Sampe, 2009: Indian Ocean capacitor effect on Indo–western Pacific climate during the summer following El Niño. *J. Climate*, **22**, 730–747, doi:10.1175/2008JCLI2544.1.

——, Y. Du, G. Huang, X.-T. Zheng, H. Tokinaga, K. Hu, and Q. Liu, 2010: Decadal shift in El Niño influences on Indo–western Pacific and East Asian climate in the 1970s. *J. Climate*, **23**, 3352–3368, doi:10.1175/2010JCLI3429.1.

Zhang, L., and T. Zhou, 2015: Drought over East Asia: A review. *J. Climate*, **28**, 3375–3399, doi:10.1175/JCLI-D-14-00259.1.

Zhu, C., B. Wang, W. Qian, and B. Zhang, 2012: Recent weakening of northern East Asian summer monsoon: A possible response to global warming. *Geophys. Res. Lett.*, **39**, L09701, doi:10.1029/2012GL051155.